Construction of Low Dissipative High Order Well-Balanced Filter Schemes for Non-Equilibrium Flows

Wei Wang[*], H. C. Yee[†], Björn Sjögreen[‡], Thierry Magin[*], and Chi-Wang Shu[§]

November 9, 2009

Abstract

The goal of this paper is to generalize the well-balanced approach for non-equilibrium flow studied by Wang et al. [26] to a class of low dissipative high order shock-capturing filter schemes and to explore more advantages of well-balanced schemes in reacting flows. The class of filter schemes developed by Yee et al. [30], Sjögreen & Yee [24] and Yee & Sjögreen [35] consist of two steps, a full time step of spatially high order non-dissipative base scheme and an adaptive nonlinear filter containing shock-capturing dissipation. A good property of the filter scheme is that the base scheme and the filter are stand alone modules in designing. Therefore, the idea of designing a well-balanced filter scheme is straightforward, i.e., choosing a well-balanced base scheme with a well-balanced filter (both with high order). A typical class of these schemes shown in this paper is the high order central difference schemes/predictor-corrector (PC) schemes with a high order well-balanced WENO filter. The new filter scheme with the well-balanced property will gather the features of both filter methods and well-balanced properties: it can preserve certain steady state solutions exactly; it is able to capture small perturbations, e.g., turbulence fluctuations; it adaptively controls numerical dissipation. Thus it shows high accuracy, efficiency and stability in shock/turbulence interactions. Numerical examples containing 1D and 2D smooth problems, 1D stationary contact discontinuity problem and 1D turbulence/shock interactions are included to verify the improved accuracy, in addition to the well-balanced behavior.

Key words: High order filter methods, WENO schemes, well-balanced schemes, non-equilibrium flow, chemical reactions, 1D turbulence/shock interactions.

1 Introduction

Recent progress in the development of a class of low dissipative high order filter schemes for multiscale Navier-Stokes and magnetohydrodynamics (MHD) systems [30, 37, 24, 32, 23, 33, 34, 35] shows good performance in multiscale shock/turbulence simulations.

The highly parallelizable high order filter methods consist of two steps, a full time step of spatially high order non-dissipative (or very low dissipative) base scheme and an adaptive

[*]Center for Turbulence Research, Stanford University, Stanford, CA 94305
[†]NASA Ames Research Center, Moffett Field, CA 94035
[‡]Lawrence Livermore National Laboratory, Livermore, CA 94551.
[§]Division of Applied Mathematics, Brown University, Providence, RI 02912

multistep filter. The nonlinear filter consists of the products of wavelet based flow sensors and the dissipative portion of high order shock-capturing schemes. The built-in flow sensors in the post processing filter step can control the amount and types of numerical dissipation only where needed, and leave the rest of the flow region free from numerical dissipation. Only the filter step might involve the use of flux limiters and approximate Riemann solvers as stabilizing mechanisms to remove Gibb's phenomena related spurious oscillations resulting from the base scheme step at locations where needed. The more scales that are resolved by the base scheme, the less the filter is utilized, thereby gaining accuracy and computational time. The adaptive numerical dissipation control idea is very general and can be used in conjunction with spectral, spectral element, finite element, discontinuous Galerkin, finite volume and finite difference spatial base schemes. The type of shock-capturing schemes used as nonlinear dissipation can be the dissipative portion of any high resolution TVD, MUSCL, ENO, or WENO shock-capturing methods [30, 11, 21]. By design, the flow sensors, spatial base schemes and linear and nonlinear dissipation models are stand alone modules. Therefore, a whole class of low dissipative high order schemes can be derived at ease.

In the recent paper by Wang et al. [26], well-balanced finite difference WENO schemes and second-order TVD schemes were studied for chemical non-equilibrium flows, extending the well-balanced finite difference WENO schemes for shallow water equations in [27, 28]. A well-balanced scheme [13], which can preserve certain nontrivial steady state solutions exactly, may help minimize some of the oscillations around steady states. It was also shown in [26] that the well-balanced schemes capture small perturbations of the steady state solutions with high accuracy. While general schemes can only resolve perturbations at the level of truncation error with the specific grid, well-balanced schemes can resolve much smaller perturbations, usually at 1% or lower of the main steady state flow.

In this paper the same approach will be applied to construct a high order well-balanced filter scheme for one temperature non-equilibrium flow with reaction terms. The multi-dimensions hyperbolic system of conservation laws with source terms (also called a balance law)

$$U_t + \nabla \cdot F(U) = S(U) \tag{1}$$

is considered, where U is the solution vector, $F(U)$ is the convective flux and $S(U)$ is the source term. For this type of flow the space variable $\mathbf{x}$ does not appear explicitly in the source term. Thus, the construction of well-balanced schemes can easily go from one-dimension to multi-dimensions.

The designing of well-balanced filter schemes is to choose a well-balanced base scheme and a well-balanced filter part. Then, the filter scheme is almost well-balanced everywhere except at the interfaces of the filtered region and the non-filtered region (see Sec. 5). Note that in this paper, a 'well-balanced filter scheme' refers to such almost well-balancedness. For the filter scheme without the flow sensor, the resulting filter scheme is well-balanced.

The choice of the sensor will not destroy the well-balanced properties. It has been shown in the previous work [26] that linear schemes, second-order Predictor-Corrector (PC) scheme [31, 14] with TVD filters (such as Harten-Yee TVD filter [29, 30]) and WENO-Roe schemes are well-balanced for certain steady state solutions with zero velocity. A well-balanced WENO-LF scheme has also been constructed for this type of steady state solutions. High order PC schemes are linear schemes and thus well-balanced. Therefore, the new filter schemes CENTVDfi/CENWENOfi or PCTVDfi/PCWENOfi which utilize central/PC schemes as the

base schemes and the Harten-Yee TVD filter or the balanced WENO schemes as the filter will be well-balanced.

In this paper, only the "zero velocity" steady state of the reacting flow will be considered in the numerical tests. Zero velocity steady state means the velocity is zero which will also imply that the flow has constant pressure and stay in chemical equilibrium. It will be shown that same as the well-balanced WENO schemes, well-balanced filter schemes give machine round-off errors regardless of the mesh sizes for the stationary steady state solutions of the reactive flow. Consequently, they can resolve small perturbations of such steady state solutions well with very coarse meshes.

Since the regular high order low dissipative filter schemes are designed for shock/turbulence interactions and the well-balanced schemes can capture small perturbations of the steady state solutions with high accuracy, the new well-balanced filter schemes take the advantages of both, thereby making them well suited for computations of turbulent fluctuations on a mainly steady flow field.

The outline of the paper is at follows: in Sec. 2, the governing equations and physical model are described. The high order filter schemes and well-balanced schemes are reviewed in Sec. 3 and 4. Then the proposed high order well-balanced filter scheme is introduced in Sec. 5. Numerical examples will be shown in Sec. 6. Finally, Sec. 7 is the conclusion and future work. A brief description of high order PC schemes and the considered time discretization are presented in the Appendix.

2 Governing equations and physical model

Considering an atmospheric entry flow in chemical nonequilibrium and thermal equilibrium, the thermodynamic properties account for excitation of the electronic states for the atoms and molecules, using the rigid-rotor harmonic-oscillator approximation for the molecules [15, 18].

Assuming neither dissipative effects nor radiation, the considered physical model is a system of hyperbolic conservation laws with source terms denoted by

$$U_t + \nabla \cdot F(U) = S(U), \tag{2}$$

$$U = \begin{pmatrix} \rho_1 \\ \cdots \\ \rho_{n_s} \\ \rho\mathbf{u} \\ \rho e \end{pmatrix}; \quad F(U) = \begin{pmatrix} \rho_1\mathbf{u} \\ \cdots \\ \rho_{n_s}\mathbf{u} \\ \rho\mathbf{u}\mathbf{u} + pI \\ (\rho e + p)\mathbf{u} \end{pmatrix}; \quad S(U) = \begin{pmatrix} s^1 \\ \cdots \\ s^{n_s} \\ \mathbf{0} \\ 0 \end{pmatrix}; \tag{3}$$

where n_s is the number of species, ρ_s, the mass density of species s, $\mathbf{u}$, the velocity vector, and e, the internal energy per unit mass of the mixture. The mixture mass density is defined as $\rho = \sum_{s=1}^{n_s} \rho_s$, and the pressure p is given by the perfect gas law

$$p = RT \sum_{s=1}^{n_s} \frac{\rho_s}{M_s}, \tag{4}$$

where R is the universal gas constant, and M_s, the molar mass of species s. The temperature T can be found from the total energy

$$\rho e = \sum_{s=1}^{n_s} \rho_s e_s(T) + \frac{1}{2}\rho|\mathbf{u}|^2, \tag{5}$$

where the internal energy e_s of species s is a function of temperature

$$\begin{aligned} e_s(T) &= e_s^T(T) + e_s^E(T) + e_s^F, \quad s \in H_a, & (6)\\ e_s(T) &= e_s^T(T) + e_s^E(T) + e_s^R(T) + e_s^V(T) + e_s^F, \quad s \in H_p, & (7) \end{aligned}$$

where H_a is the set of atoms and H_p is the set of molecules. The translational energy of species s is given by

$$e_s^T(T) = \frac{3}{2}\frac{R}{M_s}T, \tag{8}$$

and the electronic energy contribution by

$$e_s^E(T) = \frac{R}{M_s}\frac{\sum_n g_{s,n}^E \theta_{s,n}^E \exp\left(\frac{-\theta_{s,n}^E}{T}\right)}{\sum_n g_{s,n}^E \exp\left(\frac{-\theta_{s,n}^E}{T}\right)}, \tag{9}$$

where quantities $g_{s,n}^E$ and $\theta_{s,n}^E$ stand for the degeneracy and characteristic temperature of the electronic level n of species s. The number of electronic levels retained is limited for mathematical and physical standpoints. The partition function leading to thermodynamic properties diverges when all levels are accounted for. The maximum number of electronic levels of each atom and molecule is progressively increased up to a correspondence between the values of computed enthalpies and accurate reference tables. For molecule s, the rotational energy is assumed to be described by means of a rigid rotor model

$$e_s^R(T) = \frac{RT}{M_s}, \tag{10}$$

and the vibrational energy, by means of a harmonic oscillator model

$$e_s^V(T) = \frac{R}{M_s}\frac{\theta_s^V}{\exp\left(\frac{\theta_s^V}{T}\right) - 1}, \tag{11}$$

where the quantity θ_s^V stands for the vibrational characteristic temperature of the diatomic molecule. To account for the energy released in the gas by chemical reactions between the species, a common level from which all the energies are measured is established by using the formation enthalpy e_s^F at 0^oK.

The source term $S(U)$ describes the chemical reactions occurring in gas flows which result in changes in the amount of mass of each chemical species. In the general case there are J reactions of the form

$$\nu'_{1,j}X_1 + \nu'_{2,j}X_2 + \cdots + \nu'_{n_s,j}X_{n_s} \rightleftharpoons \nu''_{1,j}X_1 + \nu''_{2,j}X_2 + \cdots + \nu_{n_s,j}X_{n_s}, \quad j = 1, \ldots, J, \tag{12}$$

where $\nu'_{1,j}$ and $\nu''_{1,j}$ are respectively the stoichiometric coefficients for the reactants and products of species i in the jth reaction. For non-equilibrium chemistry the rate of production of species i due to chemical reaction may be written as

$$s^i = M_i \sum_{j=1}^{J} (\nu''_{i,j} - \nu'_{i,j}) \left[k_{f,j} \prod_{s=1}^{n_s} \left(\frac{\rho_s}{M_s} \right)^{\nu'_{s,j}} - k_{b,j} \prod_{s=1}^{n_s} \left(\frac{\rho_s}{M_s} \right)^{\nu''_{s,j}} \right], \quad i = 1, \ldots, n_s. \tag{13}$$

For each reaction j the forward and backward reaction rate coefficients, $k_{f,j}$ and $k_{b,j}$ are assumed to be known functions of temperature. The forward reaction rate coefficient is given by an Arrhenius law. Following microreversibity the backward rate coefficient is obtained from the expression $k_{f,j} = k_{b,j}/K_{e,j}$, where the equilibrium constant for the jth reaction is given by the relation

$$\ln K_{e,j} = -\frac{1}{k_{\mathrm{BT}}} \sum_{s=1}^{n_s} [(\nu''_{s,j} - \nu'_{s,j}) m_s g_s(p_{ref}, T)], \tag{14}$$

where the reference pressure $p_{ref} = 1$ Pa. The Gibbs free energy g_s of species s is a function of pressure and temperature

$$g_s(p,T) = g_s^T(p,T) + g_s^E(T), \quad s \in H_a, \tag{15}$$

$$g_s(p,T) = g_s^T(p,T) + g_s^E(T) + g_s^R(T) + g_s^V(T), \quad s \in H_p. \tag{16}$$

The translational Gibbs free energy is obtained from

$$g_s^T(p,T) = \frac{RT}{M_s} \ln \left[\frac{RT}{N_A p} \left(\frac{2\pi M_s RT}{N_A^2 h_P^2} \right)^{\frac{3}{2}} \right], \tag{17}$$

where the symbol h_P stands for Planck's constant, and N_A for Avogadro's number. The electronic Gibbs free energy reads

$$g_s^E(T) = -\frac{RT}{M_s} \ln \left[\sum_n g_{s,n}^E \exp \left(\frac{-\theta_{s,n}^E}{T} \right) \right]. \tag{18}$$

For the diatomic molecule s, the rotational Gibbs free energy is

$$g_s^R(T) = -\frac{RT}{M_s} \ln \left(\frac{T}{\theta_s^R \sigma_s} \right), \tag{19}$$

where symbol σ_s stands for the steric factor. The vibrational Gibbs free energy is obtained from the relation

$$g_s^V(T) = \frac{RT}{M_s} \ln \left[1 - \exp \left(\frac{-\theta_s^V}{T} \right) \right]. \tag{20}$$

3 Description of high order filter methods

For simplicity, the numerical methods for the 1D case is described. Denote $A = \partial F/\partial U$, the Jacobian matrix of the flux in Eq. (3). The eigenvalues of A are

$$(a^1, \ldots, a^m) = (u, \ldots, u, u + c, u - c), \tag{21}$$

where m is the number of components of vector U, $m = n_s+2$ in 1D case. c is the frozen speed of sound defined by the expression $c^2 = (\kappa+1)p/\rho$ with quantity $\kappa = (\sum_{s=1}^{n_s} \rho_s R/M_s)/(\sum_{s=1}^{n_s} \rho_s c_{v,s})$ based on the species specific heat $c_{v,s} = de_s/dT$. Denote R as the matrix whose columns are eigenvectors of A (not to be confused with the R in Eq. (4)). Let $a^l_{j+1/2}, R_{j+1/2}$ denote the quantities a^l and R evaluated at some symmetric average of U_j and U_{j+1}, such as Roe's average [22]. Define

$$\alpha_{j+1/2} = R^{-1}_{j+1/2}(U_{j+1} - U_j) \tag{22}$$

as the difference of the local characteristic variables in the x direction.

The low dissipative high order filter scheme developed by Yee et al. [30] suggests using the artificial compression method of Harten [7] as a flow sensor to limit the amount of numerical dissipation that is inherent in a scheme. Subsequently, Sjögreen and Yee [24], Yee and Sjögreen [33, 35] introduced a wavelet decomposition of the data to determine the location where numerical dissipation is needed. The considered filter method contains two steps, a high order low dissipative spatial base scheme step (not involving the use of approximate Riemann solvers or flux limiters) and a multistep filter (usually involving the use of approximate Riemann solvers and flux limiters). The nonlinear filter consists of the product of a wavelet (WAV) sensor [24] and the nonlinear dissipative portion of a high-resolution shock-capturing scheme.

We will briefly review the high order filter schemes in this section. For more details, we refer the readers to [30, 24, 33, 35].

3.1 High order spatial scheme step

The first step of the numerical method consists of a time step via a high order non-dissipative spatial and high order temporal base scheme operator L^*. After the completion of a full time step of the base scheme, the solution is denoted by U^*

$$U^* = L^*(U^n), \tag{23}$$

where U^n is the numerical solution vector at time level n.

The high order non-dissipative spatial base schemes could be the standard central schemes, the centered compact scheme or the predictor-corrector (PC) schemes [31, 14].

For strong shock interactions and/or steep gradient flows, a small amount of high order linear dissipation can be added to the base scheme step to reduce the time step constraint and stability. For example, an eighth-order linear dissipation with the sixth-order central scheme to approximate $F(U)_x$ is written as

$$\frac{\partial F}{\partial x} \approx D_{06}\, F_j + d(\Delta x)^7 (D_+ D_-)^4 U_j, \tag{24}$$

where D_{06} is the standard sixth-order accurate centered difference operator, and D_+D_- is the standard second-order accurate centered approximation of the second derivative. The small parameter d is a scaled value (e.g., spectral radius of $A(U)$) in the range of 0.00001-0.0005, depending on the flow problem, and has the sign which gives dissipation in the forward time direction. See Appendix for more choices of spatial base schemes.

3.2 Adaptive nonlinear filter step (discontinuities and high gradient capturing)

After the completion of a full time step of the high order base scheme, the second step is to adaptively filter the solution by the product of a "wavelet sensor" and the "nonlinear dissipative portion of a high-resolution shock-capturing scheme" (involving the use of flux limiters). The final update step after, e.g., the nonlinear filter step can be written as

$$U_j^{n+1} = U_j^* - \frac{\Delta t}{\Delta x}\left[H^{fx}_{j+1/2} - H^{fx}_{j-1/2}\right]. \tag{25}$$

Here, the filter numerical fluxes

$$H^{fx}_{j+1/2} = R_{j+1/2}\bar{H}_{j+1/2}. \tag{26}$$

Denote the elements of the vector $\bar{H}_{j+1/2}$ by $\bar{h}^l_{j+1/2}$, $l = 1, 2, \ldots m$. The nonlinear portion of the filter $\bar{h}^l_{j+1/2}$ has the form

$$\bar{h}^l_{j+1/2} = \frac{1}{2}(s^N)^l_{j+1/2}(\phi^l_{j+1/2}). \tag{27}$$

Here, $(s^N)^l_{j+1/2}$ is the sensor to activate the higher order nonlinear numerical dissipation $\phi^l_{j+1/2}$. $(s^N)^l_{j+1/2}$ is designed to be zero or near zero in regions of smooth flow and near one in regions with discontinuities. $(s^N)^l_{j+1/2}$ varies from one grid point to another and is obtained from a wavelet analysis of the flow solution [24]. The wavelet sensor can be obtained from the characteristic variables for each wave or a single sensor for all waves, based on pressure and density. The latter one is used in the paper.

The dissipative portion of the nonlinear filter $\phi^l_{j+1/2} = g^l_{j+1/2} - b^l_{j+1/2}$ is the dissipative portion of a high order high-resolution shock-capturing scheme for the local l-th characteristic wave. Here $g^l_{j+1/2}$ and $b^l_{j+1/2}$ are numerical fluxes of the uniformly high order high-resolution scheme and a high order central scheme for the l-th characteristic wave, respectively.

For the numerical examples, two forms of nonlinear dissipation $\phi^l_{j+1/2}$ were considered, namely:

- Dissipative portion of balanced WENO schemes (see Sec. 4). It is obtained by taking the full WENO scheme and subtracting the central scheme, such as, WENO5-D_{06} and WENO7-D_{08}.
- Dissipative portion of the Harten-Yee TVD scheme [29, 30].

Remark 1. *In [35], Yee and Sjögreen proposed and studied both linear and nonlinear filters, where the linear filters refer to the standard spectral filter, compact filter and non-compact high order linear numerical dissipation. In our paper, only nonlinear filters, especially the dissipative portion of WENO and TVD schemes are considered.*

Remark 2. *Yee and Sjögreen also did comparisons of applying the filters between "after each Runge-Kutta stage" and "after a full time step". Their research indicated that there is no advantage of applying the filters "after each Runge-Kutta stage". In addition, "after a full time step" is extremely efficient since only one Riemann solve per time step per dimension is required.*

3.3 Flow sensor by multiresolution wavelet analysis of the computed flow data

A general description of how to obtain different flow sensors (e.g., $(s^N)^l_{j+1/2}$) by multiresolution wavelet analysis of the computed flow data can be found in Sjögreen and Yee [24] and Yee and Sjögreen [32].

The wavelet flow sensor estimates the Lipschitz exponent of a grid function f_j (e.g., the density and pressure). The Lipschitz exponent at a point x is defined as the largest α satisfying

$$\sup_{h\neq 0} \frac{|f(x+h)-f(x)|}{h^\alpha} \leq C, \tag{28}$$

and this gives information about the regularity of the function f, where small α means poor regularity. For a C^1 wavelet function w with compact support α can be estimated from the wavelet coefficients, defined as

$$w_{m,j} = \langle f, \psi_{m,j} \rangle = \int f(x)\psi_{m,j}(x)dx, \tag{29}$$

where

$$\psi_{m,j} = 2^m \psi\left(\frac{x-j}{2^m}\right) \tag{30}$$

is the wavelet function $\psi_{m,j}$ on scale m located at the point j in space. In practical computations we have a smallest scale determined by the grid size. We evaluate $w_{m,j}$ on this scale, m_0, and a few coarser scales, m_0+1, m_0+2, and estimate the Lipschitz exponent at the point j_0 by a least square fit to the line [24]

$$\max_{j \text{ near } j_0} \log_2 |w_{m,j}| = m\alpha + c. \tag{31}$$

A continuous function $f(x)$ has a Lipschitz exponent $\alpha > 0$. A bounded discontinuity (shock) has $\alpha = 0$, and a Dirac function (local oscillation) has $\alpha = -1$. Large values of k can be used in turbulent flow so that large vortices or vortex sheets can be detected.

For more details about the wavelet and the flow sensor, we refer the readers to [24, 35].

4 Description of well-balanced methods

A well-balanced scheme refers to a scheme that preserves exactly specific steady state solutions of the governing equations. In the previous work [26] the linear schemes, WENO-Roe scheme, Harten-Yee TVD and the Predictor-Corrector TVD schemes (with zero entropy correction) are proven theoretically and numerically to be well-balanced schemes for the non-equilibrium flow Eq. (2) with zero velocity steady states. We will briefly review the idea of the well-balancedness in this section.

For the general 1-D system balance law

$$U_t + F(U,x)_x = S(U,x), \tag{32}$$

the steady state solution U satisfies

$$f^l(U,x)_x = s^l(U,x), \quad l = 1,\dots,m, \tag{33}$$

where f^l and s^l are the lth elements of the vectors $F(U,x)$ and $S(U,x)$.

A linear finite-difference operator D is defined to be one satisfying $D(af_1+bf_2) = aD(f_1)+bD(f_2)$ for constants a, b and arbitrary grid functions f_1 and f_2. A scheme for Eq. (32) is said to be a linear scheme if all the spatial derivatives are approximated by linear finite-difference operators.

As proved in [27], under the following two assumptions regarding Eq. (32) and the steady state solution of Eq. (33), linear schemes with certain restrictions are well-balanced schemes. Furthermore, high-order nonlinear WENO schemes can be adapted to become well-balanced schemes.

Assumption 1. *The considered steady state preserving solution U of Eq.* (33) *satisfies*

$$r_s(U,x) = \textit{constant}, \quad s = 1,2,\dots \tag{34}$$

for a finite number of known functions $r_s(U,x)$.

Assumption 2. *Each component of the source term vector $S(U,x)$ can be decomposed as*

$$s^l(U,x) = \sum_i \tau_i(r_1(U,x), r_2(U,x),\dots)\, t_i'(x), \quad l = 1,\dots,m, \tag{35}$$

for a finite number of functions τ_i and t_i, where τ_i could be arbitrary functions of $r_s(U,x)$, and τ_i and t_i can be different for different $s^l(U,x)$. (Here t_i is not to be confused with the time "t" indicated on all previous conservation laws.)

Now consider the non-equilibrium flow Eq. (2). First, since $S(U,x) \equiv S(U)$, all the $t_i'(x) = 1$. Next, when the flow is in the steady state, the chemistry is in equilibrium and thus the source vector $S(U) = 0$. Therefore, two assumptions are easily satisfied by taking

$$r_i(U) = s^i(U), \quad i = 1,\dots,m. \tag{36}$$

Furthermore, linear schemes (such as central and PC schemes) and WENO-Roe scheme are naturally well-balanced for such steady state solutions of Eq. (2) (see [26]).

A well-balanced finite difference WENO-LF scheme can be constructed with a limiter λ in the Lax-Friedrichs flux splitting

$$f^{\pm}(u) = \frac{1}{2}(f(u) \pm \alpha\lambda u). \tag{37}$$

λ is close to 0 or 1 according to the solution which is in steady state or away from steady state. In particular, λ is constructed by

$$\begin{aligned} \lambda := \quad & \max\left(\min\left(1, \frac{(|r_1(U_{i+1},x_{i+1})-r_1(U_i,x_i)|+|r_1(U_{i-1},x_{i-1})-r_1(U_i,x_i)|)^2}{|r_1(U_{i+1},x_{i+1})-r_1(U_i,x_i)|^2+|r_1(U_{i-1},x_{i-1})-r_1(U_i,x_i)|^2+\varepsilon}\right),\right. \\ & \left.\min\left(1, \frac{(|r_2(U_{i+1},x_{i+1})-r_2(U_i,x_i)|+|r_2(U_{i-1},x_{i-1})-r_2(U_i,x_i)|)^2}{|r_2(U_{i+1},x_{i+1})-r_2(U_i,x_i)|^2+|r_2(U_{i-1},x_{i-1})-r_2(U_i,x_i)|^2+\varepsilon}\right),\dots\right), \end{aligned} \tag{38}$$

where ε is a small number to avoid zero in the denominator and we take it as 10^{-6} in the computations. Near the specific steady state, the differences in r_i shown in (38) are close to zero. λ will be near zero when all these differences are small compared with ε. λ is near one if the solution is far from the steady state, since the differences in r_i shown in (38) are now on the level of $O(\Delta x)$ and much larger than ε, and then the scheme is the regular WENO-LF scheme. The limiter does not affect the high order accuracy of the scheme in smooth region for general solutions of Eq. (2). In the specific steady state, since all the r_i are constants, λ becomes zero and then the scheme maintains the exact solutions for such steady state.

We remark that the functions r_i in the limiter (38) are used to distinguish the states between steady and unsteady. They are not necessarily to be the same as in Assumption 1, but they must be a necessary condition for the steady states. For example, in the considered "zero velocity" steady state, zero velocity will imply zero source terms and constant pressure etc. $u = 0$ is a necessary condition for zero velocity steady state. Thus taking $\lambda := \left(\min\left(1, \frac{(|v(U_{i+1},x_{i+1})|+|v(U_i,x_i)|)^2}{|v(U_{i+1},x_{i+1})|^2+|v(U_i,x_i)|^2+\varepsilon}\right)\right.$ also works in the code implementation.

The dissipative portion of the TVD schemes has the form

$$\phi^l_{j+1/2} = \frac{1}{2}\left[\psi(\nu^l_{j+1/2}) - (\nu^l_{j+1/2})^2\right]\left(\alpha^l_{j+1/2} - \hat{Q}^l_{j+1/2}\right), \tag{39}$$

where

$$\nu^l_{j+1/2} = \frac{\Delta t}{\Delta x} a^l_{j+1/2}, \tag{40}$$

$a_{j+1/2}$ and $\alpha_{j+1/2}$ are defined in (21) and (22).

The function $\psi(z)$ is an entropy correction to $|z|$ (see [29]) with

$$\psi(z) = \begin{cases} |z| & |z| \geq \delta_1 \\ (z^2 + \delta_1^2)/2\delta_1 & |z| < \delta_1 \end{cases}, \tag{41}$$

where δ_1 is the entropy fix parameter (see [36] for a discussion). $\hat{Q}^l_{j+1/2}$ is an unbiased limiter function which can be

$$\hat{Q}^l_{j+1/2} = \text{minmod}(\alpha^l_{j-1/2}, \alpha^l_{j+1/2}) + \text{minmod}(\alpha^l_{j+1/2}, \alpha^l_{j+3/2}) - \alpha^l_{j+1/2} \tag{42}$$

with

$$\text{minmod}(a, b) = \text{sgn}(a) \cdot \max\{0, \min[|a|, b\,\text{sgn}(a)]\}. \tag{43}$$

It has been proven in [26] that the zero velocity steady state solution, $R_{j+1/2}\bar{H}_{j+1/2}$ in Eq. (26) maintains zero and thus can be used as the filter part for the well-balanced filter schemes.

5 High order well-balanced filter scheme

The construction of high order well-balanced filter schemes is rather straightforward. The first step is to choose any well-balanced scheme, such as central scheme (CENx), PCx (here x denotes the number 2, 4, 6 or 8) or any linear scheme as base scheme. The second step is to choose a well-balanced filter, such as the dissipative portion of the TVD scheme (39) or the high order well-balanced WENO scheme.

Here, we would like to remark that these constructed filter schemes are well-balanced, except at the interface between the filtered and non-filtered regions. Because in the interface of these two regions, the numerical fluxes get information from different schemes (base scheme part and filter part), the schemes will not be well-balanced at those interface cells. This is not a serious concern, since the interface is only a small portion of the whole computational domain. Also, since the filter is turned on only at the shock region, the transition region of the shock is usually far away from the considered zero velocity steady state. Thus, there is no need to require the schemes to be well-balanced at the interfaces.

Also note that the linear dissipation part $d(\Delta x)^7(D_+D_-)^4U_j$ in the base scheme (24) cannot preserve the steady state solutions. Similar to LF flux, since there are no assumptions on the density functions, the dissipation $d(\Delta x)^7(D_+D_-)^4U_j$ may produce non-zero values in the steady states. Here, the same idea of constructing well-balanced WENO-LF schemes is applied, i.e., multiplying a limiter λ (38) to the linear dissipation part to turn off the linear dissipation in the steady state area. Since the linear dissipation is only needed for stability concern before reaching steady state, numerical tests show that turning it off by the limiter λ does not affect the stability of the solution. With the limiter λ, the filter schemes will have no linear dissipation in the steady state and thus will maintain the exact steady state solutions.

In this paper the considered well-balanced filter schemes are low order central filter schemes with TVD filter (CEN2TVDfi and CEN4TVDfi), and high order central filter schemes with balanced WENO filter (CEN6WENO5fi and CEN8WENO7fi). Similar considered PC filter schemes are PC2TVDfi, PC4TVDfi, PC6WENO5fi and PC8WENO7fi. For the same order PC & central filter schemes, the accuracies are similar. Comparing to central filter schemes, PC filter schemes allow a larger CFL number for time integration. However, the PC filter schemes only allow 1st & 2nd-order time discretizations. The central filter schemes allow a wider class of time discretizations.

6 Reaction model and test cases

In this section, the gas model for sub-orbital Earth reentries comprising five species N_2, O_2, NO, N, and O is described. Then, different numerical tests of the considered high order well-balanced filter schemes for one- and two- dimensional reacting flows are performed. The first example is to numerically verify that the constructed filter schemes are well-balanced by time-marching on a nontrivial steady state. In this test the well-balanced filter schemes will show round-off numerical errors for a specific steady state solution. The second example is a small perturbation over the steady state. We can observe the well-balanced filter schemes showing their advantage in resolving the perturbations in very coarse meshes. For 1D numerical tests, we show three additional examples involving shocks. The first one is a stationary contact discontinuity problem, where the left and right states of the discontinuity are both in equilibrium. We will show that if there are small perturbations on the two sides of the discontinuity, the well-balanced schemes can capture them very accurately. The second shock example is a 1D turbulence/shock interaction problem where only the right state of the shock is in equilibrium. If there are small perturbations on the right of the shock, the well-balanced schemes will well resolve them, then when the shock passes through those perturbations, well-balanced schemes will have more accurate results than the non well-balanced scheme on the left of the shock. The third example is a shock tube problem to test the shock-capturing capability of the considered

schemes. There numerical test cases are to demonstrate that well-balanced schemes will not destroy the non-oscillatory shock resolution away from the steady state.

6.1 Reaction model

The air mixture comprises 5 species, N_2, O_2, NO, N, and O, with elemental fractions 79% for nitrogen and 21% for oxygen. The spectroscopic constants used in the computation of the species thermodynamic properties (θ_s^V, $\theta_{s,n}^E$, θ_s^R, g_s^E in Sec. 2) and the formation enthalpies are obtained from Gurvich et al. [6]. The chemical mechanism comprises three dissociation recombination reactions for molecules

$$N_2 + M \rightleftharpoons 2N + M, \quad \text{(see [20])} \tag{44}$$

$$O_2 + M \rightleftharpoons 2O + M, \quad \text{(see [20])} \tag{45}$$

$$NO + M \rightleftharpoons N + O + M, \quad \text{(see [19])} \tag{46}$$

where M is a catalytic particle (any of the species N_2, O_2, NO, N, and O), and two Zeldovich reactions for NO formation

$$N_2 + O \rightleftharpoons NO + N, \quad \text{(see [2])} \tag{47}$$

$$O_2 + N \rightleftharpoons NO + O, \quad \text{(see [3])}. \tag{48}$$

6.2 One dimensional numerical results

6.2.1 Well-balanced test

The purpose of the first test problem is to numerically verify the well-balanced property of the proposed filter schemes. The special zero velocity stationary case with

$$T = 1000 \times (1 + 0.2\sin(\pi x))K, \quad p = 10^5\ N/m^2, \quad u = 0\ m/s, \tag{49}$$

is considered. The initial composition is based on the local thermodynamic equilibrium (LTE) assumption. Given Eq. (49) and the source term $S(U) = 0$, each species is uniquely determined.

Eq. (49) is chosen as the initial condition which is also the exact steady state solution, and the results are obtained by time-accurate time-marching on the steady state. The computational domain is $[-1, 1]$. The L^1 relative errors of temperature at $t = 0.01$ (about 1000 time steps for $N = 100$ grid points) are listed in Table 1. The L_1 relative error is measured to be the difference between the exact solution Eq. (49) and the numerical solution divided by the L_1 norm of the exact solution.

Table 1 shows that the considered high order central filter schemes and PC filter schemes are well-balanced because they produce errors at the level of machine round-off errors in double precision.

Table 1: L^1 relative errors for temperature by central/PC filter schemes at $t = 0.01$.

N	error	error	error	error
	CEN2TVDfi	CEN4TVDfi	CEN6WENO5fi	CEN8WENO7fi
50	3.84E-11	3.84E-11	3.79E-11	3.67E-11
100	3.79E-11	3.79E-11	3.68E-11	3.62E-11
	PC2TVDfi	PC4TVDfi	PC6WENO5fi	PC8WENO7fi
50	3.83E-11	3.76E-11	3.69E-11	3.63E-11
100	3.88E-11	3.85E-11	3.81E-11	3.78E-11

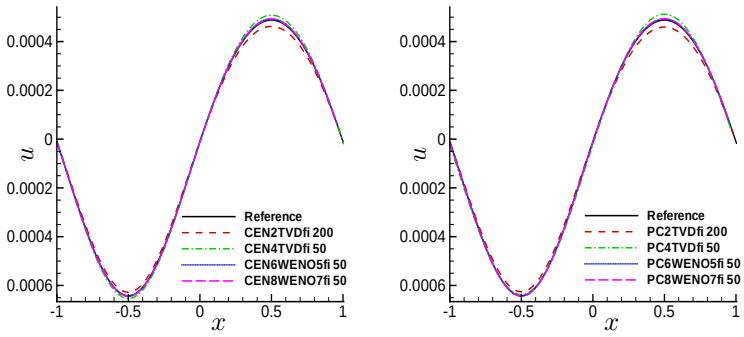

Figure 1: Small perturbation of velocity results by filter schemes: $\epsilon = 10^{-3} \times \sin(\pi x)$. Left: central filter schemes; Right: PC filter schemes.

6.2.2 Small perturbation

The following test problem will demonstrate the advantages of well-balanced schemes through the problem of a small perturbation over a stationary state.

The same stationary solution, Eq. (49), is considered. A small perturbation $\epsilon = 10^{-3} \times \sin(\pi x)$ is added to the velocity, i.e.,

$$u' = u + \epsilon. \tag{50}$$

The other quantities are kept unperturbed. Figs. 1 show the velocities by central and PC filter schemes of orders 2, 4, 6 and 8 at $t = 0.1$. The reference results are computed by fifth order WENO-Roe with 1200 points and are considered to be "exact".

The results show that all the considered high order well-balanced filter schemes can capture the small perturbation well in a very coarse mesh. Especially for the schemes with order higher than 2, only 50 points are used. However, the non well-balanced schemes behave in a very oscillatory fashion, such as WENO-LF, without the limiter lambda in (38), with 200 points (Fig. 2). They can only resolve the solution when the mesh is refined enough such that the truncation error of the scheme is much smaller than the perturbation.

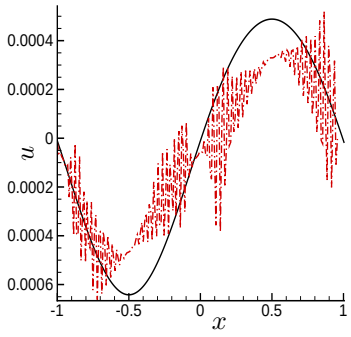

Figure 2: Small perturbation of velocity results by WENO-LF scheme: $\epsilon = 10^{-3} \times \sin(\pi x)$. WENO-LF 200 points: dash-dot; Reference 1200 points: solid).

6.2.3 1D stationary contact discontinuity problem

The third example is a 1D stationary contact discontinuity problem on the domain $[-5, 5]$. A stationary contact discontinuity is located at $x = 0$. The flow contains zero velocity and constant pressure $20N/m^2$ everywhere. The temperature has an initial condition

$$T = \begin{cases} 500 \times (1 + 0.1\sin(2\pi x)), & x < 0 \\ 300 \times (1 + 0.1\sin(2\pi x)), & x > 0 \end{cases} . \tag{51}$$

The densities for each species can be solved by LTE condition. We add a small perturbation of the velocity over the whole domain

$$u' = u + 0.05 \times \sin(\pi x). \tag{52}$$

The computation stops at time $t = 0.01$. We remark that the solutions were computed on a larger domain $[-6, 6]$ but truncated on $[-5, 5]$ for not considering the effects by the boundary condition. Figs. 3 and 4 show the densities, temperatures, velocities and pressures by the balanced WENO-LF scheme and the regular WENO-LF scheme with 100 cells. The reference solution is computed by the WENO-Roe scheme with 1200 cells. From the Figs. 3 we can see that the balanced WENO-LF produces a more accurate result than the regular WENO-LF scheme. The regular WENO-LF scheme has a discrepancy from the reference solution on the waves and it cannot capture the small wave close to the shock. Unlike the density and temperature, the velocity and pressure are constant at the initial time. Thus it is more clear to see the difference between the balanced WENO-LF and the regular WENO-LF on the velocity and pressure results. From Figs. 4, we can see the results by the balanced WENO-LF are undistinguished from the reference solution. However, the regular WENO-LF produces large oscillations due to the truncation errors.

Figs. 5 and 6 show the results by the central filter schemes. The considered central filter schemes here are CEN2TVDfi and CEN4TVDfi with 200 cells, and CEN6WENO5fi and CEN8WENO7fi with 100 cells. All the well-balanced central schemes can capture the small

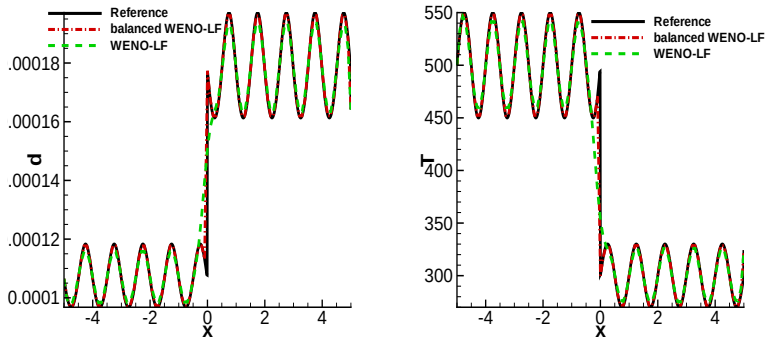

Figure 3: 1D stationary contact discontinuity problem by WENO-LF schemes with 100 cells: left: density of O_2; right: temperature.

perturbations very well. Figs. 7 and 8 show the results by PC filter schemes. The considered PC filter schemes here are PC2TVDfi, PC4TVDfi, PC6WENO5fi and PC8WENO7fi with 200 cells. We remark that the PC scheme we implemented seems losing accuracy due to the boundary or the time discretization. Thus for some PC filter schemes we use a more refined mesh than the same order of the central filter schemes. But we will try to fix it in the future. The well-balanced PC filter schemes can capture the small perturbations well except a small wave around $x = -2$ in the pressure plot (right subfigure of Figs. 8). This is because the well-balanced filter schemes are almost well-balanced everywhere except the transition areas between the filter part and non-filter part which are not well-balanced (see Sec. 5). The small wave will be resolved when the mesh is more refined.

6.2.4 1D shock/turbulence interaction problem

The fourth example is a 1D Shu-Osher problem for reacting flows on the domain $[-5, 5]$. Initially a shock is located at $x = -4$. The shock is moving at the speed $500m/s$ to the right. The right state of the flow consists two parts, the first part is a constant equilibrium state from -4 to 1 and the second part is an oscillatory equilibrium state from 1 to 5 with sine waves in densities and temperature. The conditions are given by

$$(T_R, p_R, v_R) = \begin{cases} (500, 20, 0), & x \in [-4, 1] \\ (500 \times (1 + 0.1\sin(2\pi x)), 20, 0), & x \in [1, 5] \end{cases}. \tag{53}$$

Given the temperature and pressure, the densities for each species at the LTE state can be uniquely determined by the LTE condition. The left equilibrium state can be calculated according to the Rankine-Hugoniot jump condition.

Since the right state of the flow is a zero velocity LTE state, the well-balanced schemes can solve it with machine round-off errors. If we add a small perturbation of the velocity all over the right state

$$u' = u + 10^{-3} \times \sin(\pi x), \quad x \in [-4, 5], \tag{54}$$

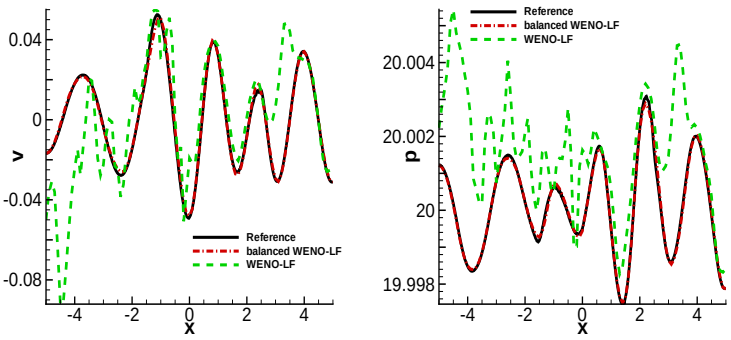

Figure 4: 1D stationary contact discontinuity problem by WENO-LF schemes with 100 cells: left: velocity; right: pressure.

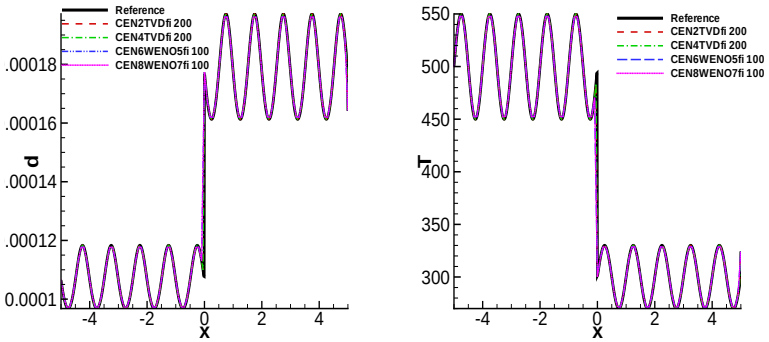

Figure 5: 1D stationary contact discontinuity problem by central filter schemes: left: density of O_2; right: temperature.

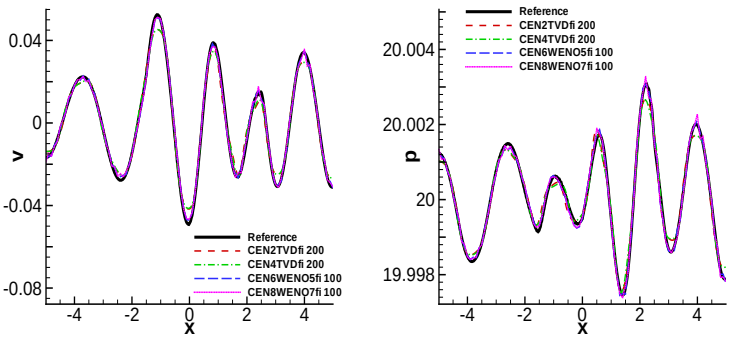

Figure 6: 1D stationary contact discontinuity problem by central filter schemes: left: velocity; right: pressure.

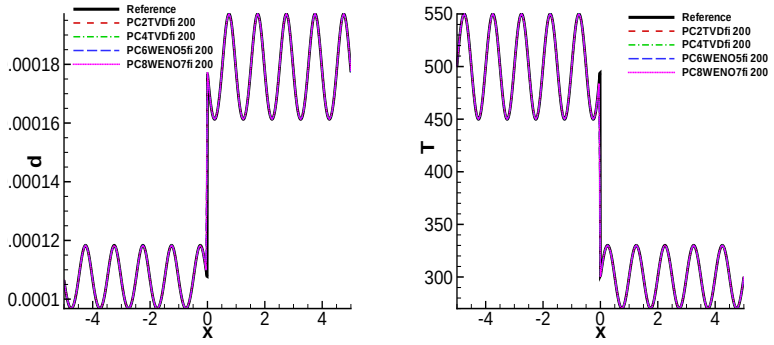

Figure 7: 1D stationary contact discontinuity problem by PC filter schemes: left: density of O_2; right: temperature.

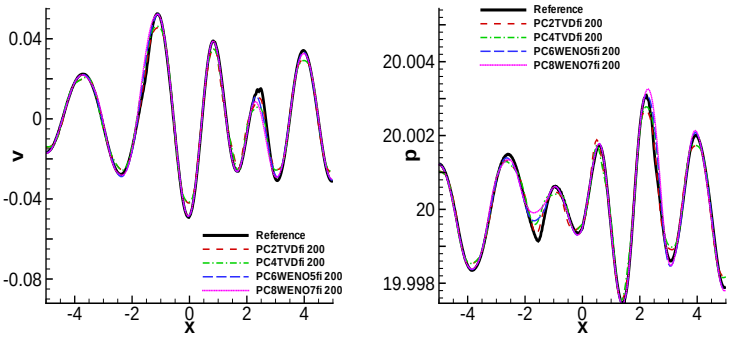

Figure 8: 1D stationary contact discontinuity problem by PC filter schemes: left: velocity; right: pressure.

the well-balanced schemes will be able to capture this small perturbation very well.

At time equal to 0.012 seconds, the shock moves to $x = 2$. The shock first passed through the small perturbation of the velocity and then passed through one sine wave (at the region $x \in [1, 2]$).

The reference solution is computed by WENO-Roe with 2000 cells. Figs. 9 and 10 show the comparison of the regular 5th order WENO-LF scheme and the balanced 5th order WENO-LF scheme on velocity and pressure with 100 cells. From the global views of velocity and pressure (the left subplots of Figs. 9 and 10), we hardly see any differences between these two schemes. However, if zooming in the region $[-5, 1]$, we can see the balanced WENO-LF scheme can capture the small perturbation very well whereas the regular WENO-LF scheme which is not well-balanced schemes cannot do that (the right subplots of Figs. 9 and 10). The density and temperature results by WENO-LF schemes are also shown in Figs. 11.

The results by central and PC filter schemes are shown in Figs. 12, 13, 14, 15, 16 and 17. We remark that for the strong shock problem, the filter schemes cannot be essentially non-oscillatory around the shocks (although the oscillations are hardly seen from the global views). The well-balanced schemes are proposed to have advantages for the region close to the steady state, so we only focus on the regions away from the shocks ($x \in [-5, -2]$). The considered central filter schemes here are CEN2TVDfi and CEN4TVDfi with 300 cells, and CEN6WENO5fi and CEN8WENO7fi with 100 cells. The considered PC filter schemes here are PC2TVDfi and PC4TVDfi with 300 cells, and PC6WENO5fi and PC8WENO7fi with 200 cells. Because for the moving shock problem, the filtered region is moving with the shock, and the switches between filtered and unfiltered will cause non well-balancedness, so the results of moving shock in this section are not so impressive as the results of stationary contact discontinuity in Sec. 6.2.3. We use a more refined mesh for low order schemes CEN2TVDfi, CEN4TVDfi, PC2TVDfi and PC4TVDfi. High order schemes CEN6WENO5fi and CEN8WENO7fi with 100 cells have underresolved solutions in the crest and trough of the waves. PC6WENO5fi and PC8WENO7fi with a more refined mesh 200 cells can resolve them better.

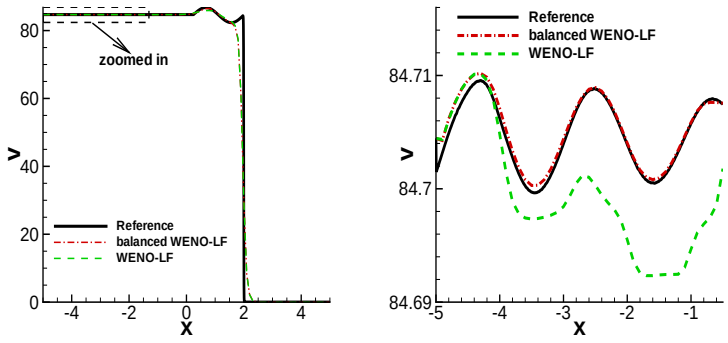

Figure 9: 1D Shu-Osher problem of velocity results by WENO-LF schemes with 100 cells: left: global; right: zoomed in.

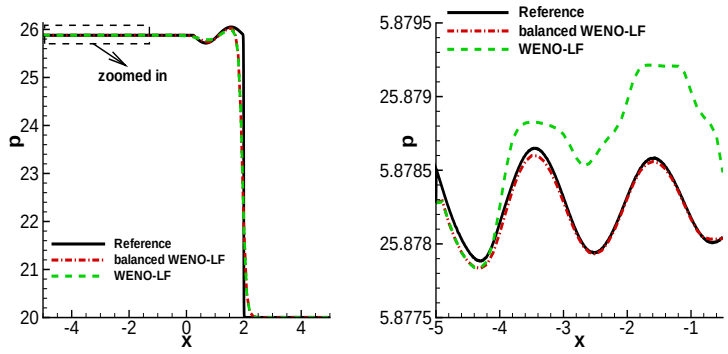

Figure 10: 1D Shu-Osher problem of pressure results by WENO-LF schemes with 100 cells: left: global; right: zoomed in.

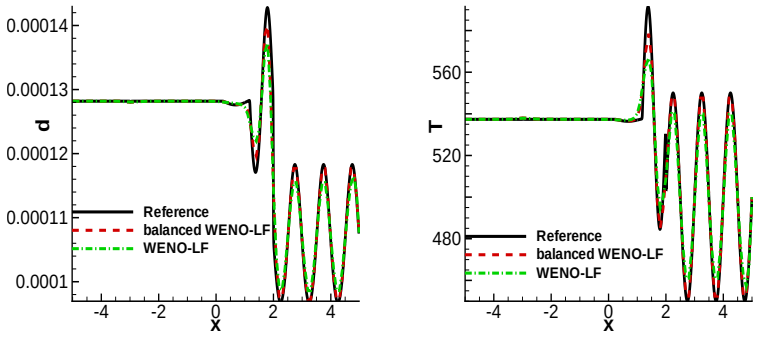

Figure 11: 1D Shu-Osher problem by WENO-LF schemes with 100 cells: left: density; right: temperature.

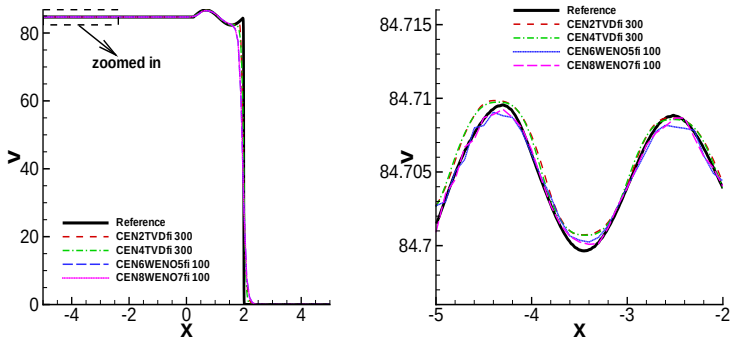

Figure 12: 1D Shu-Osher problem of velocity results by central filter schemes: left: global; right: zoomed in.

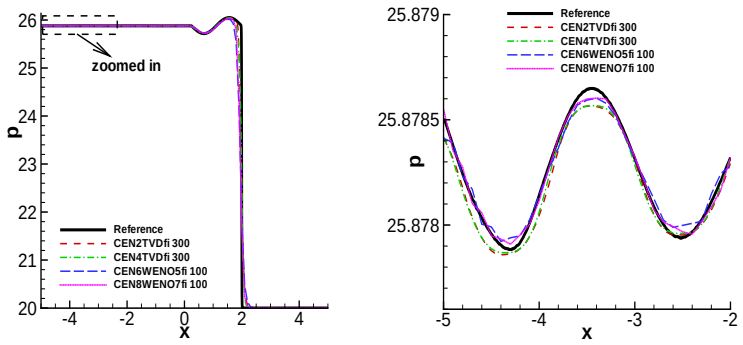

Figure 13: 1D Shu-Osher problem of pressure results by central filter schemes: left: global; right: zoomed in.

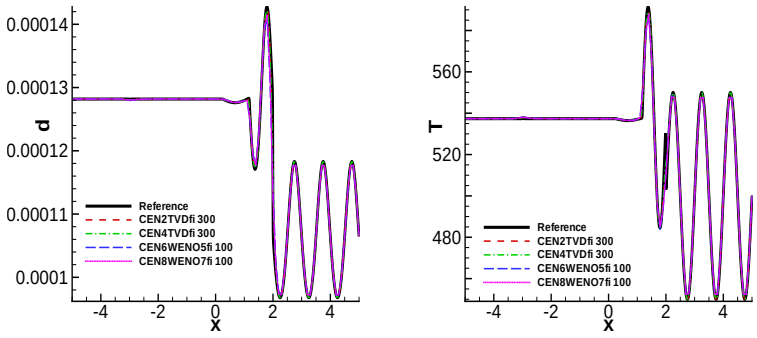

Figure 14: 1D Shu-Osher problem by central filter schemes: left: density; right: temperature.

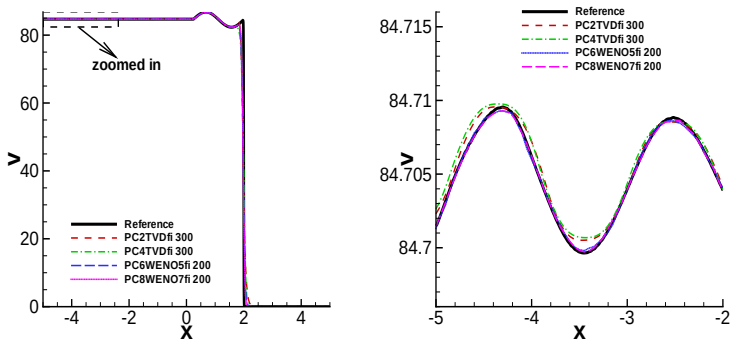

Figure 15: 1D Shu-Osher problem of velocity results by PC filter schemes: left: global; right: zoomed in.

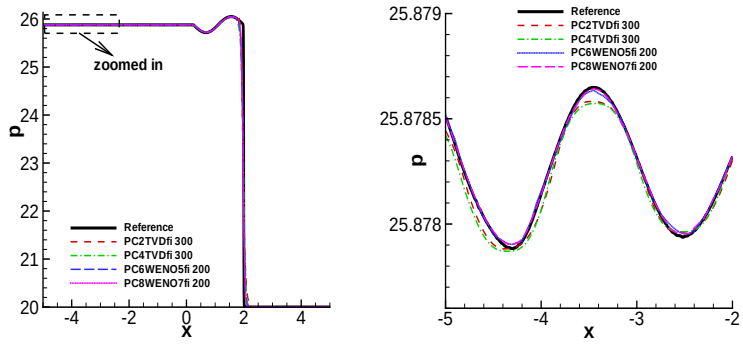

Figure 16: 1D Shu-Osher problem of pressure results by PC filter schemes: left: global; right: zoomed in.

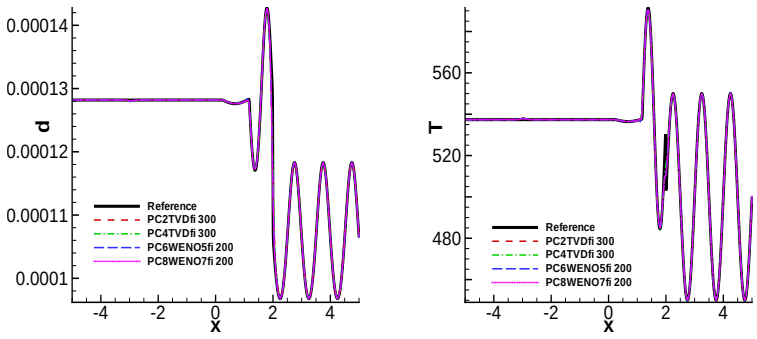

Figure 17: 1D Shu-Osher problem by PC filter schemes: left: density; right: temperature.

6.2.5 A shock tube problem

The last 1D example is a shock tube problem. A diaphragm is located at $x = 0$ which separates the right chamber from the left chamber. The right chamber has cold air with pressure $0.6 \times 10^5 N/m^2$ and temperature 300K. The gas in the left chamber has high pressure $6 \times 10^5 N/m^2$ and high temperature 3000K. Both gases are in LTE condition. The computational domain is $[-5, 5]$ in the lab frame.

The results are computed at $t = 0.001$. The solution is no longer in steady state. This example is to test the shock capturing ability of our well-balanced filter schemes. The numerical results of temperature, velocity and mass fraction of N_2 (from left to right) computed by CEN6WENO5fi, CEN8WENO7fi, PC6WENO5fi and PC8WENO7fi are plotted in Figs. 18, 19, 20 and 21. As expected, the rarefaction wave, contact surface and shock appear in the temperature solution. Since the velocity is consistent through the contact surface, thus there are only rarefaction wave and shock appearing in the velocity solution. Furthermore, mass is conserved during the shock. No shock appears in the mass solution. All the considered well-balanced filter schemes can capture the shocks sharply without oscillations.

6.3 Two dimensional numerical results

As mentioned in the beginning, extending the well-balanced schemes to the zero velocity steady state of 2D reacting flow is trivial because the reacting term does not explicitly depend on the dimensions. In this section, similar well-balanced tests to 2D reacting flow will be performed.

6.3.1 2D Well-balanced test

Similar to 1D, the first example is to check that our scheme maintains the 2D zero velocity steady state exactly. The 2D special stationary case

$$T = 1000 \times (1 + 0.2 \sin(\pi(x + y)))K, \quad p = 10^5 \ N/m^2, \quad \mathbf{u} = \mathbf{0} \ m/s, \tag{55}$$

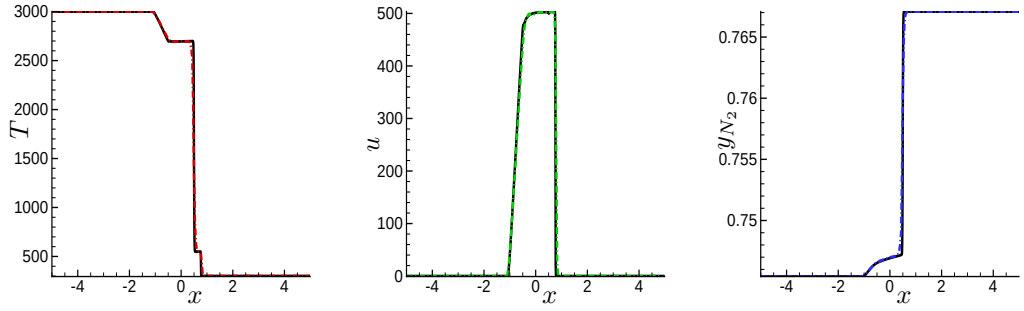

Figure 18: Shock tube problem by CEN6WENO5fi: Left: temperature; Middle: velocity; Right: mass fraction of N_2 (CEN6WENO5fi with 300 points: dash-dot; Reference 1200 points: solid).

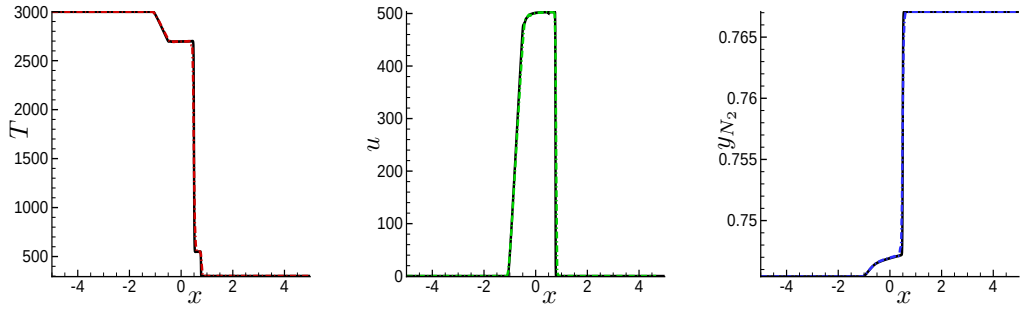

Figure 19: Shock tube problem by CEN8WENO7fi: Left: temperature; Middle: velocity; Right: mass fraction of N_2 (CEN8WENO7fi with 300 points: dash-dot; Reference 1200 points: solid).

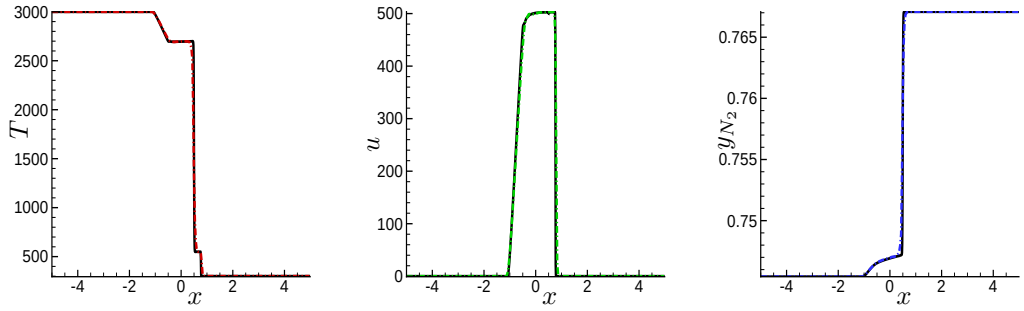

Figure 20: Shock tube problem by PC6WENO5fi: Left: temperature; Middle: velocity; Right: mass fraction of N_2 (PC6WENO5fi with 300 points: dash-dot; Reference 1200 points: solid).

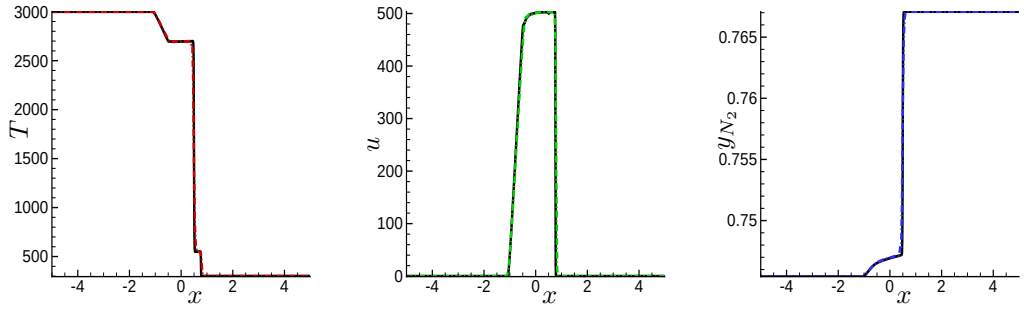

Figure 21: Shock tube problem by PC8WENO7fi: Left: temperature; Middle: velocity; Right: mass fraction of N_2 (PC8WENO7fi with 300 points: dash-dot; Reference 1200 points: solid).

Table 2: L^1 relative errors for temperature by central/PC schemes at $t = 0.01$.

$N \times N$	error	error	error	error
	CEN2TVDfi	CEN4TVDfi	CEN6WENO5fi	CEN8WENO7fi
50×50	4.14E-11	4.14E-11	4.21E-11	4.30E-11
100×100	4.04E-11	3.69E-11	3.73E-11	3.82E-11
	PC2TVDfi	PC4TVDfi	PC6WENO5fi	PC8WENO7fi
50×50	4.13E-11	4.20E-11	4.24E-11	4.29E-11
100×100	4.03E-11	4.07E-11	4.10E-11	4.13E-11

is considered. The computation is performed to $t = 0.01$ (about 2000 time steps for 100×100 grid points) on the domain $[-1, 1]^2$. Table 2 shows the L^1 relative errors for the temperature T. We can clearly see that the L^1 relative errors are at the level of round-off errors, verifying the well-balancedness of the considered central filter and PC filter schemes for 2D reacting flow.

6.3.2 2D small perturbation test

The second example is again a small perturbation test but on a 2D steady state. The same 2D steady state solution Eq. (55) is considered. A small perturbation $\epsilon = 10^{-3} \times \sin(\pi(x + y))$ is added to the velocity in the x direction, i.e.,

$$u' = u + \epsilon. \tag{56}$$

The other quantities are kept unperturbed. The reference solution is computed by WENO-Roe scheme with 200×200 points. Fig. 22 show the contours of velocity by 2nd order central/PC TVD filter schemes at $t = 0.01$. The results by sixth and eighth central/PC WENO filter schemes are shown in Figs. 23 and 24. The 1D cross-section results by PC filter schemes, central filter schemes and WENO-LF are shown in Fig. 25 left, middle and right subplots separately. We can see that our well-balanced filter schemes can capture the small perturbation in a coarse

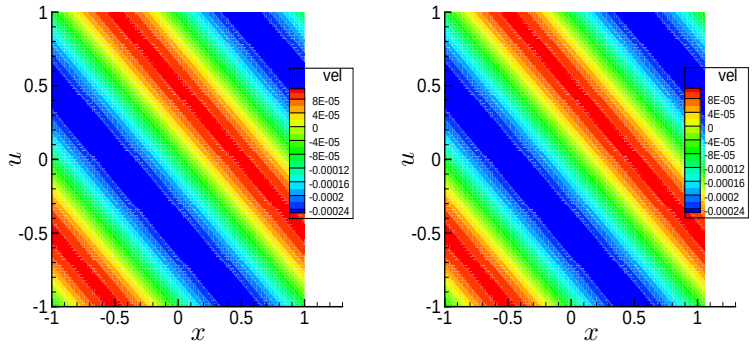

Figure 22: 2D small perturbation of velocity results by filter schemes: $\epsilon = 10^{-3} \times \sin(\pi(x+y))$. Left: CEN2TVDfi 100×100 points; right: PC2TVDfi 100×100 points.

mesh very well (especially for the schemes with order higher than 2 where only 40×40 is used). However, the WENO-LF produces large oscillations even in a mesh 100×100 (right subplots of Fig. 25).

7 Concluding remarks

In this paper the well-balanced approach is extended to the high order filter schemes in solving five species reacting flow in one and two space dimensions. Numerical examples are given to demonstrate the well-balanced property, accuracy, good capturing of the small perturbation of the steady state solutions, and the non-oscillatory shock resolution of the proposed well-balanced filter schemes. Because of the property of the zero velocity steady state solution of the reacting flow, the extension to any number of species and other reaction models is straighforward. Future research will consider the non-zero velocity steady state and the advantages of well-balanced schemes to various steady state problems.

Acknowledgments

The authors acknowledge the support of the DOE/SciDAC SAP grant DE-AI02-06ER25796. The work by Björn Sjögreen is performed under the auspices of the U.S. Department of Energy by Lawrence Livermore National Laboratory under Contract DE-AC52-07NA27344 LLNL-JRNL-409903.

8 Appendix: Predictor-Corrector schemes and other spatial base schemes

Samples of the high-order base schemes for F_x can be of the following types.
Central differencings:

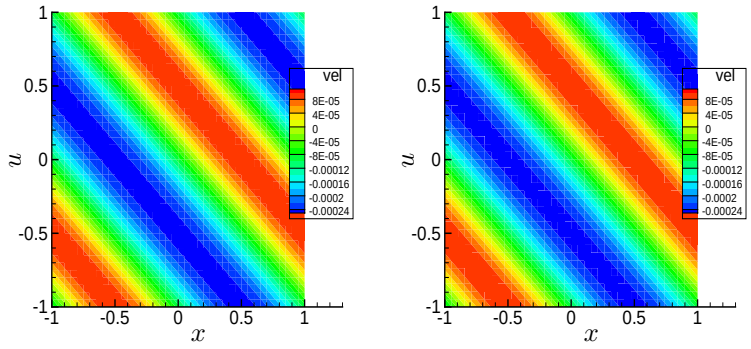

Figure 23: 2D small perturbation of velocity results by central filter schemes: $\epsilon = 10^{-3} \times \sin(\pi(x+y))$. Left: CEN6WENO5fi 40×40 points; right: CEN8WENO7fi 40×40 points.

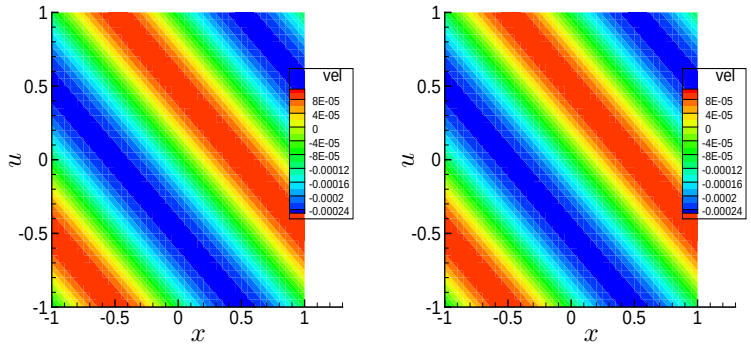

Figure 24: 2D small perturbation of velocity results by PC filter schemes: $\epsilon = 10^{-3} \times \sin(\pi(x+y))$. Left: PC6WENO5fi 40×40 points; right: PC8WENO7fi 40×40 points.

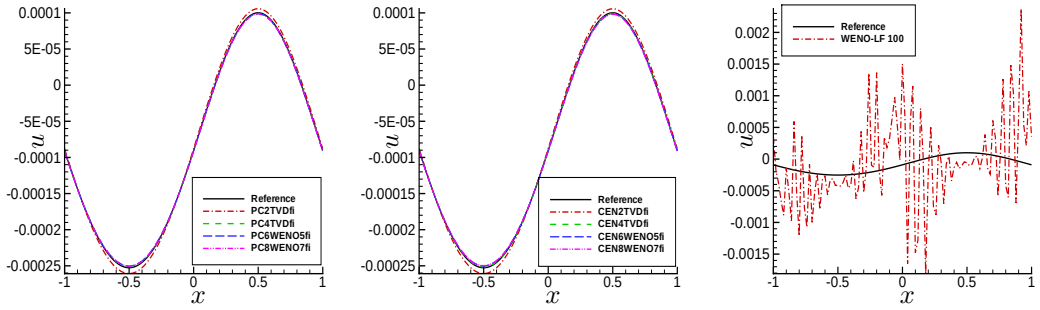

Figure 25: Cross section of 2D velocity results at $y = 0$: $\epsilon = 10^{-3} \times \sin(\pi(x+y))$. Left: central filter schemes; middle: PC filter schemes; right: WENO-LF.

CEN4:

$$F_x \approx \frac{1}{12\Delta x}(F_{j+2} - 8F_{j+1} + 8F_{j-1} - F_{j-2}), \tag{57}$$

CEN6:

$$F_x \approx \frac{1}{60\Delta x}(F_{j+3} - 9F_{j+2} + 45F_{j+1} - 45F_{j-1} + 9F_{j-2} - F_{j-3}). \tag{58}$$

Compact central differencings (Hirsh [8], Ciment and Leventhal [4], and Lele [12]). Here

$$F_x \approx \frac{1}{\Delta x}(A_x^{-1} B_x F)_j, \tag{59}$$

where for a fourth-order approximation

$$\begin{array}{rcl} (A_x F)_j & = & \frac{1}{6}(F_{j+1} + 4F_j + F_{j-1}), \\ (B_x F)_j & = & \frac{1}{2}(F_{j+1} - F_{j-1}), \end{array} \tag{60}$$

and a sixth-order approximation

$$\begin{array}{rcl} (A_x F)_j & = & \frac{1}{5}(F_{j+1} + 3F_j + F_{j-1}), \\ (B_x F)_j & = & \frac{1}{60}(F_{j+2} + 28F_{j+1} - 28F_{j-1} - F_{j-2}). \end{array} \tag{61}$$

Predictor-corrector differencings:
PC4:

$$\begin{array}{rcl} D_p F_j & = & \frac{1}{6\Delta x}\left(7F_j - 8F_{j-1} + F_{j-2}\right), \\ D_c F_j & = & \frac{1}{6\Delta x}\left(-7F_j + 8F_{j+1} - F_{j+2}\right), \end{array} \tag{62}$$

PC6:

$$\begin{array}{rcl} D_p F_j & = & \frac{1}{30\Delta x}\left(37F_j - 45F_{j-1} + 9F_{j-2} - F_{j-3}\right), \\ D_c F_j & = & \frac{1}{30\Delta x}\left(-37F_j + 45F_{j+1} - 9F_{j+2} + F_{j+3}\right), \end{array} \tag{63}$$

and PC8:

$$\begin{array}{rcl} D_p F_j & = & \frac{1}{420\Delta x}\left(533F_j - 672F_{j-1} + 168F_{j-2} - 32F_{j-3} + 3F_{j-4}\right), \\ D_c F_j & = & \frac{1}{420\Delta x}\left(-533F_j + 672F_{j+1} - 168F_{j+2} + 32F_{j+3} - 3F_{j+4}\right), \end{array} \tag{64}$$

where D_pF is the PC differencing operator approximating F_x at the first step (predictor step) and D_cF is the PC differencing operator at the second step (corrector step). New forms of the upwind biased PC methods including compact formulations developed by Hixon and Turkel [9, 10] are also applicable as spatial base schemes. Interested readers should refer to their paper for the various upwind-biased PC formulae. The choice of the time integrators for these types of PC methods is more limited. For example, if second-order time accuracy is desired, then (62), (63) and (64) in conjunction with the appropriate second-order Runge-Kutta method are analogous to the familiar 2-4, 2-6 and 2-8 MacCormack schemes developed by Gottlieb and Turkel [5] and Bayliss et al. [1]. Here the first number refers to the order of accuracy for the time discretization and the second number refers to the order of accuracy or the spatial discretization. However, in this case one achieves the second-order time accuracy without dimensional splitting of the Strang type [25]. For higher than second-order time discretizations, only certain even stage Runge-Kutta methods are applicable. For compatible fourth-order Runge-Kutta time discretizations, see Hixon and Turkel for possible formulae. For example, the classical fourth-order Runge-Kutta is applicable provided one applies the predictor and the corrector step twice for the four stages, i.e., the predictor step for the first and third stages and the corrector step for the second and fourth stages.

For the considered 1D system with source term (2), the predictor-corrector scheme with 2nd-order implicit explicit Runger-Kutta in time takes the form

$$U^{(1)} = U^n - \Delta t D_p F(t^n, U^n) + \Delta t S(t^n, U^n), \tag{65}$$

$$U^{n+1} = ((U^{(1)} + U^n) - \Delta t D_c F(t^{n+1}, U^{(1)}) + \Delta t S(t^{n+1}, U^{n+1}))/2, \tag{66}$$

The PC operators are modified at boundaries in a stable way by the summation-by-part (SBP) operators [17, 16, 32]. If D_b is the standard *pth* order SBP for the centered difference operators, then the *pth* order PC operators are modified in this way

$$F_x \approx \begin{cases} D_p F_j, & j = b+1, \ldots, N \\ (D_b - D_c)F_j, & j = 1, \ldots, b \end{cases} \tag{67}$$

at the predictor step and

$$F_x \approx \begin{cases} D_c F_j, & j = 1, \ldots, N-b \\ (D_b - D_p)F_j, & j = N-b+1, \ldots, N \end{cases} \tag{68}$$

at the corrector step, where N is the number of grids and b is the number of points needed at boundaries.

References

[1] Bayliss, A., Parikh, P., Maestrello, L. & Turkel, E 1985 A fourth-order scheme for the unsteady compressible Navier Stokes equations, *ICASE Report No. 85-44.*

[2] Bose, D. & Candler, G.V. 1996 Thermal rate constants of the N_2+O→ NO+N reaction using ab initio $^3A''$ and $^3A'$ potential energy surfaces *J. Chem. Phys.* **104**, 2825–2833.

[3] Bose, D. & Candler, G.V. 1997 Thermal rate constants of the O_2+N→ NO+O reaction based on the $^2A'$ and $^4A'$ potential-energy surfaces *J. Chem. Phys.* **107**, 6136–6145.

[4] Ciment, M. & Leventhal, H. 1975 Higher order compact implicit schemes for the wave equation, *Math Comp.* **29**, 985–994.

[5] Gottlieb, D & Turkel, E 1976 Dissipative twofour methods for time dependent problems, *Math Comp.* **30**, 703–723.

[6] Gurvich, L.V., Veits, I.V. & Alcock, C.B. 1989 Thermodynamic properties of individual substances, volume 1: O, H/D,T/, F, Cl, Br, I, He, Ne, Ar, Kr, Xe, Rn, S, N, P, and their compounds, Part one: methods and computation, Part two: tables *New York, Hemisphere Publishing Corp., 1989.*

[7] Harten, A. 1978 The artificial compression method for computation of shocks and contact discontinuities: III. Self-adjusting hybrid schemes, *Math. Comp.* **32**, 363–389.

[8] Hirsh, R. S. 1975 Higher order accurate difference solutions of fluid mechanics problems by a compact differencing technique, *J. Comp. Phys.* **19**, 90–109.

[9] Hixon, R. & Turkel, E. 1998 High-accuracy compact MacCormack-type schemes for computational aeroacoustics, *AIAA-1998-365, Aerospace Sciences Meeting and Exhibit, 36th, Reno, NV, Jan. 12-15, 1998*

[10] Hixon, R. & Turkel, E. 2000 Compact implicit MacCormack-type schemes with high accuracy, *J. Comp. Phys.* **158**, 51–70.

[11] Jiang, G. & Shu, C.-W. 1996 Efficient implementation of weighted ENO schemes, *J. Comp. Phys.* **126**, 202–228.

[12] Lele, S. 1992 Compact nite difference schemes with spectral-like resolution, *J. Comp. Phys.* **103**, 16–42.

[13] LeVeque, R. J. 1998 Balancing source terms and flux gradients in high-resolution Godunov methods: the quasi-steady wave-propagation algorithm, *J. Comp. Phys.* **146**, 346–365.

[14] LeVeque, R. J. & Yee, H. C. 1990 A study of numerical methods for hyperbolic conservation laws with stiff source terms, *J. Comp. Phys.* **86**, 187–210.

[15] Magin, T. E., Caillault, L., Bourdon, A., & Laux, C. O. 2006 Nonequilibrium radiative heat flux modeling for the Huygens entry probe, *J. Geophys. Res.* **111**, E07S12.

[16] Nordstrom, J. & Carpenter, M. H. 1999 Boundary and interface conditions for high-order finite-difference schemes applied to the Euler and Navier-Stokes equations, *J. Comp. Phys.* **148**, 621–645.

[17] Olsson, P. 1995 Summation by parts, projections and stability I, *Math. Comput.* **64**, 1035–1065.

[18] Panesi, M., Magin, T. E., Bourdon, A., Bultel, A. & Chazot, O. 2009 Analysis of the FIRE II flight experiment by means of a collisional radiative model, *J. of Thermophysics and Heat Transfer* **23**, 236–248.

[19] Park, C. 1993 Review of chemical-kinetic problems of future NASA missions. I - Earth entries *J. of Thermophysics and Heat Transfer* **7**, 385–398.

[20] Park, C., Jaffe, R.L. & Partridge, H. 2001 Chemical-kinetic parameters of hyperbolic Earth entry *J. of Thermophysics and Heat Transfer* **15**, 76–90.

[21] Qiu, J., Khoo, B. C. & Shu, C.-W. 2006 A numerical study for the performance of the Runge-Kutta discontinuous Galerkin method based on different numerical fluxes, *J. Comp. Phys.* **212**, 540–565.

[22] Roe, P. L. 1981 Approximate Riemann solvers, parameter vectors, and difference schemes, *J. Comp. Phys.* **43**, 357–372.

[23] Sjögreen, B. & Yee, H. C. Efficient low dissipative high order schemes for multiscale MHD flows, I: Basic theory, *AIAA 2003-4118, in: Proceedings of the 16th AIAA/CFD Conference, 23-26 June 2003, Orlando, FL.*

[24] Sjögreen, B. & Yee, H. C. 2004 Multiresolution wavelet based adaptive numerical dissipation control for shock-turbulence computation, *RIACS Technical Report TR01.01, NASA Ames research center (Oct 2000); J. Sci. Comp.* **20**, 211–255.

[25] Strang, G. 1968 On the construction and comparison of difference schemes, *SIAM J. Numer. Anal.* **5**, 506–517.

[26] Wang, W., Shu, C.-W., Yee, H. C.& Sjögreen, B. 2009 High order well-balanced schemes and applications to non-equilibrium flow, *J. Comp. Phys.*, **228**, 5787–5802.

[27] Xing, Y. & Shu, C.-W. 2005 High order finite difference WENO schemes with the exact conservation property for the shallow water equations, *J. Comp. Phys.* **208**, 206–227.

[28] Xing, Y. & Shu, C.-W. 2006 High order well-balanced finite difference WENO schemes for a class of hyperbolic systems with source terms, *J. Sci. Comp.* **27**, 477–494.

[29] Yee, H. C. 1989 A class of high-resolution explicit and implicit shock-capturing methods, *VKI lecture series 1989-04, March 6-10, 1989; NASA TM-101088, Feb. 1989.*

[30] Yee, H. C. , Sandham, N. D., & Djomehri, M. J. 1999 Low dissipative high order shock-capturing methods using characteristic-based filters, *J. Comp. Phys.* **150**, 199–238.

[31] Yee, H. C. & Shinn, J. L. 1989 Semi-implicit and fully implicit shock-capturing methods for nonequilibrium flows, *AIAA Journal* **225**, 910–934.

[32] Yee, H. C. & Sjögreen, B. 2001 Designing Adaptive Low Dissipative High Order Schemes for Long-Time Integrations, *"Turbulent Flow Computation", D.Drikakis and B.Geurts (eds.), October 2001* .

[33] Yee, H. C. & Sjögreen, B. 2005 Efficient low dissipative high order scheme for multiscale MHD flows, II: Minimization of Div(B) numerical error, *RIACS Technical Report TR03.10, July, 2003, NASA Ames Research Center; J. Sci. Comp.* , DOI: 10.1007/ s10915-005-9004-5.

[34] Yee, H. C. & Sjögreen, B. 2006 Nonlinear Filtering and Limiting in High Order Methods for Ideal and Non-ideal MHD, *J. Sci. Comp* **27**, 507–521.

[35] Yee, H. C. & Sjögreen, B. 2007 Development of low dissipative high order filter schemes for multiscale Navier-Stokes/MHD systems, *J. Comp. Phys.* **68**, 151–179.

[36] Yee, H. C., Sweby, P. K. & Griffiths, D. F. 1991 Dynamical approach study of spurious steady-state numerical solutions for non-linear differential equations, Part I: The dynamics of time discretizations and its implications for algorithm development in computational fluid dynamics, *J. Comp. Phys.* **97**, 249–310.

[37] Yee, H. C., Vinokur, M & Djomehri, M. J. 2000 Entropy Splitting and Numerical Dissipation, *J. Comp. Phys.* **162**, 33–81.